Renewable Energy 184 (2022) 662–676

Contents lists available at ScienceDirect

Renewable Energy

journal homepage: www.elsevier.com/locate/renene

Estimation of blade forces in wind turbines using blade root strain measurements with OpenFAST verification

Bridget Moynihan [a], Babak Moaveni [a, *], Sauro Liberatore [a, b], Eric Hines [a]

[a] Tufts University, Medford, MA, USA
[b] MIDE Technology Corporation, Woburn, MA, USA

ARTICLE INFO

Article history:
Received 23 July 2021
Received in revised form
1 November 2021
Accepted 24 November 2021
Available online 1 December 2021

Keywords:
Wind turbines
Condition monitoring
Strain sensors
Wind energy
Structural health monitoring

ABSTRACT

This paper introduces an inference method for computing the forces and bending moments on operating wind turbine blades using strain measurements and supervisory control and data acquisition (SCADA) data. Operational data from four months of a Clipper Liberty C96 2.5 MW turbine instrumented with interferometric strain sensors at the blade roots as well as SCADA data such as wind speed, rotor hub speed, and blade pitch angle allow for accurate calculation of blade forces and moments. To perform such calculations, certain structural properties of the turbine blades must be inferred in the absence of detailed, proprietary information. This is done by inferring missing information from the National Renewable Energy Laboratory (NREL) 3 MW WindPACT reference wind turbine specifications. The derived forces and moments computed on the blades of the Clipper turbine are compared with the behavior of the NREL 3 MW reference turbine according to OpenFAST simulation outputs. Comparison of blade root reaction forces to OpenFAST outputs match closely, demonstrating that this inference method can be used to successfully estimate the internal forces and bending moments acting on the blades. These methods are useful on turbines for which all the structural information is not available.

1. Introduction

Wind power additions in the U.S. continue to increase and total U.S. wind power capacity has now surpassed 120 GW, 4 times the existing operating capacity from 10 years ago [1]. Wind turbines (WT) too have continued to grow in size. The original equipment manufacturer (OEM) Siemens Gamesa recently launched the designs for a 14-MW offshore WT (OWT) with a 222-m diameter rotor [2]. This new turbine has surpassed the GE 12-MW Haliade-X, which was the world's largest OWT [3] in both size and output and had become the turbine of choice in 2019 for offshore wind developments on the U.S. Atlantic Coast.

As wind turbines (WT) continue to grow, the reliability of these massive structures is key to ensuring the availability of low-cost renewable energy [4]. Operation and maintenance (O&M) costs are one of the largest contributors to wind power's levelized cost of energy (LCOE), constituting 10–20% of the LCOE, and reaching up to 35% at the end of life [5]. O&M also reduces efficiency by causing downtime which can take up to 3% of WT and OWT total lifetimes [6].

Maintenance costs in a WT can vary considerably based on performance and failures [7], and it is important to reduce these where possible. Unplanned downtime due to corrective maintenance is problematic for WT owners [8], as it is difficult to predict and can make up 30%–60% of total O&M costs [5].

Condition based maintenance is a form of preventive maintenance which consists of regular monitoring of the WT components to detect potential faults [9] to address issues before failure occurs, reducing downtime. Condition monitoring (CM) which falls under condition-based maintenance is preferable to corrective or time-based maintenance as it reduces machine shutdown, limiting downtime and reducing energy costs [5,10].

Structural health monitoring (SHM), as a form of condition monitoring (CM), is an important tool for ensuring the integrity of structures, including WT [5,17], as it allows for maintenance before failure occurs and reduces O&M costs [6]. Some common blade SHM methods include vibration monitoring, acoustic emissions (AE), strain measurement and impedance techniques [18].

Application of SHM methods using dynamic strain measurement and vibrations is well studied but obtaining further information on the condition of WT from strain measurements can

* Corresponding author.
E-mail address: babak.moaveni@tufts.edu (B. Moaveni).

https://doi.org/10.1016/j.renene.2021.11.094
0960-1481/

make CM systems more effective and cost efficient. This has been studied through response estimation techniques used to measure fatigue at locations where sensors are not or cannot be placed, typically below the waterline of offshore WT [13,14].

Vibrational blade SHM techniques are among the most common methods to monitor blade health [16,17]. These methods analyze modal properties and natural frequencies to detect changes to the structure of the blades [18], however vibrational techniques require supplementary methods to locate and quantify the damage [15]. Accelerometers are the most common type of sensor required to carry out vibrational analysis of the blades [15].

SHM methods using strain measurements on the blades are also common; these methods are typically used for load monitoring but are also applied for damage detection [15,19]. Strain measurement for load monitoring is an important aspect for the blade pitch control system. Further, blade loads can provide insight into the best control strategies to minimize extreme loading on the blades and other components of the WT [20]. Load monitoring applications can be used by WT operators to make maintenance or repair decisions for turbines [21].

Strain measurement systems can be costly [22,23] and there are several challenges such as high sampling rate requirements, memory space, and power availability [24]. Additionally, many sensors are typically required to detect even small damages [18]. Therefore, methods to improve the cost-effectiveness of strain measurement CM systems for blades would be valuable [23,25].

Load monitoring on blades is commonly utilized by WT operators to measure two primary blade-root bending moments: the flapwise and edgewise bending moments. These blade root bending moments are useful in assessing whether the blades are overloaded [20]. Analyzing additional blade root forces and bending moments on the blades would be useful for further understanding the effects of different loading conditions on structural health [26]. Utilization of strain measurements to compute these forces and moments requires design details on the WT.

This paper introduces a method to analyze root reaction forces and moments on the blades of a Clipper Liberty C96 2.5 MW turbine instrumented with axial strain sensors at the blade roots. SCADA data from the turbine is also available and used in this analysis. This study computes root reaction forces and bending moments on the blades based on the available strain measurements. The WindPACT 3 MW reference WT [27] detailed by the National Renewable Energy Laboratory (NREL) is used to infer certain structural properties of the blades where proprietary information from manufacturers is unavailable. In the WindPACT specifications, NREL also provides descriptions of resulting forces and other parameters to be used in the design of WT. Results of this method are compared to these forces and parameters described by NREL as a function of wind speed. The NREL reference turbine used is also modeled in OpenFAST by the authors, so that more detailed comparisons of all the root reaction forces and moments with the Clipper turbine can be made.

2. Available data and data processing

The data utilized in this paper includes 4 axial strain measurements from the root of each blade. This data is of a period spanning four months of operation, with over 1500 h of data in total. SCADA data which is synchronized with the strain sensor readings is available from the same time-period. The available data is the foundation for calculation of forces and moments on the blades.

2.1. Strain sensors

The strain sensors on the Clipper 2.5 MW turbine are optical intereferometers with corresponding temperature sensors to compensate for temperature. The sensors are positioned in 4 evenly spaced locations (0°, 90°, 180°, 270°) at each blade root where the blade cross section is circular, schematically depicted in Fig. 1. The locations of the sensors are titled Low Pressure, High Pressure, Leading Edge and Trailing Edge, named after the pressure distribution due to

wind flow on the blades' airfoil cross section further along the span.

2.1.1. Strain data cleaning and temperature compensation

"Fig. 2 shows the original, cleaned, and temperature compensated data of Blade 1. The sensor output included some outliers (voltage spikes), typical of digital sensors. The outliers were removed and replaced using a cubic spline interpolation. The top plot shows the original strain readings, where a few such outliers are seen in the data. The cleaned data is shown in the second plot of Fig. 2. The sensors were then temperature compensated based on the manufacturer's parameters for strain reconstruction. The temperature compensated strain readings are shown in the bottom plot of Fig. 2. Each plot in the figure displays the four sensor readings for Blade 1 of the turbine."

2.2. Supervisory control and data acquisition (SCADA)

The synchronized SCADA data available includes more than 30 parameters of the wind turbine's operation and atmospheric conditions. This includes key measurements such as wind speed, rotor hub speed, and blade pitch angle. Table 1 details the most important available SCADA data parameters.

Fig. 3 displays example data gathered from the SCADA system. The sample rate of the SCADA data is 0.5 Hz as shown in Fig. 3, but readings were interpolated to match the sampling rate of the strain gauge data, 100 Hz.

3. Methodology

3.1. Modeling assumptions

The Clipper C96 2.5 MW WT considered in this work has a 96 m rotor diameter with blade lengths of 46.7 m and a hub height of 80 m [28]. The hub diameter is approximately 2.6 m. The strain sensors are located 1.5 m from the centerline of the main shaft, which results in forces and moments computed on the blades acting just past the blade root. Most detailed design parameters on the Clipper turbine are not publicly available.

3.1.1. NREL reference turbine

NREL publishes open-access reference wind turbines which are comprehensive designs of turbines to be used in research and

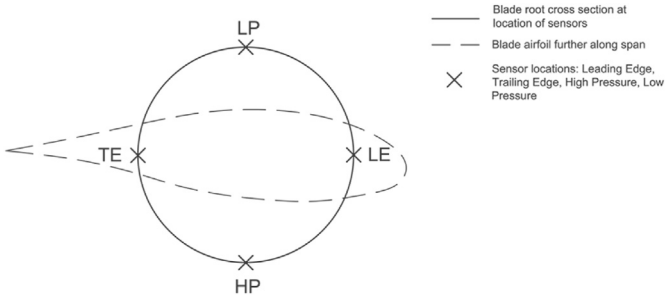

Fig. 1. Sensor location at blade roots.

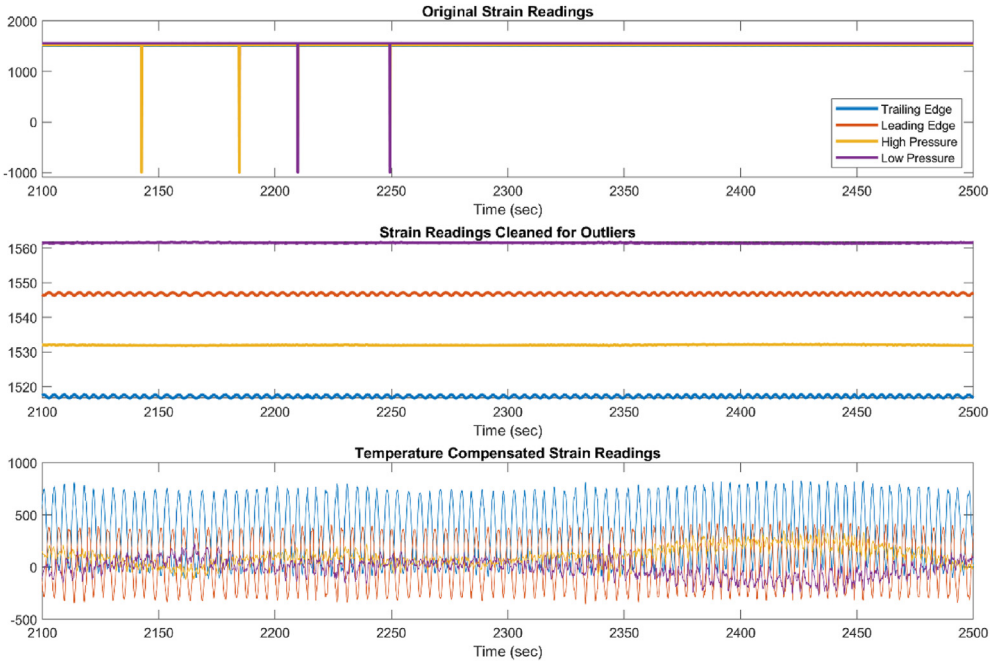

Fig. 2. Cleaned and temperature compensated strain gauge readings.

Table 1
Available SCADA data parameters for clipper 2.5 MW turbine.

SCADA Data Parameters	
Active Power	Blade 1 Torque
Air Density	Blade 2 Torque
Ambient Temp	Blade 3 Torque
Barometric Pressure	Generator Speed
Blade Rotor Angle	Hub Speed
Blade 1 Pitch Angle	Nacelle Position
Blade 2 Pitch Angle	Wind Direction
Blade 3 Pitch Angle	Wind Speed
Blade 1 Pitch Rate	Yaw Position
Blade 2 Pitch Rate	Yaw Error
Blade 3 Pitch Rate	

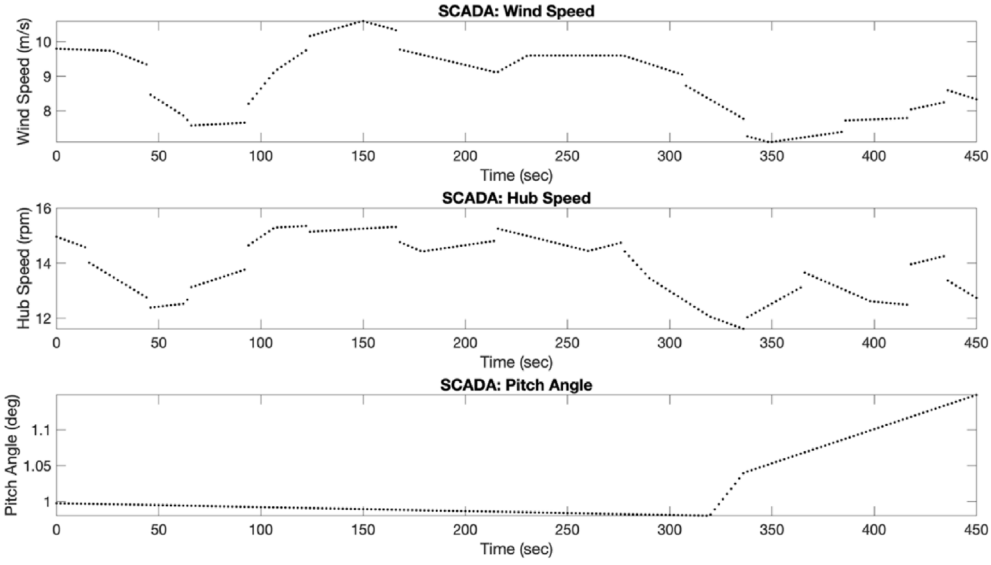

Fig. 3. SCADA system example data.

education. The NREL 3 MW WindPACT reference turbine [27] was chosen for this paper as the optimal turbine to compare to the Clipper 2.5 MW turbine. The 3 MW reference turbine is utilized to replace certain design details not available for the Clipper turbine. In particular, the blade structural properties are largely unknown for the Clipper turbine, including the airfoil profiles along the span.

Table 2 compares key properties of the NREL 3 MW reference turbine and the Clipper C96 2.5 MW turbine. The power rating of the NREL WindPACT 3.0 is 20% higher than the Clipper C96, but the rotor radius is only 3.0% larger and the blade length is only 0.69% longer. The rated wind speeds are also similar. Since this project is concerned with blade root moments, the similarity in blade geometries between these two turbines allows for reasonable blade moment comparisons with the key assumption being that the blade cross sections along the span of the blade is comparable in each turbine.

3.1.2. Local blade axes

Moments and forces on each of the blades are calculated in the local axes of the blade, represented in Fig. 4 by the three axes separated by 120°. The local axes of blades are labeled as x, y, z, while the global axes of turbine are denoted as X, Y, Z, each creating a right-handed coordinate system. The x-axis is perpendicular to span of blade, and points in the same direction as the nacelle, running parallel to and coincident with wind direction (when there is no veer). The local x-axis is always facing in the same direction as the global X-axis. The y-axis is in the plane of the blades' rotation, and the z-axis is in the axial direction along the blade.

3.1.3. Blade rotation

Fig. 4 details the rotation of the blades around the rotor, where ω is the rotational speed and r is the distance from the center of the rotor hub, where r spans from 0 to R. The horizontal speed of a point on the blade with distance r from center is ωr. The rotational speed of the rotor hub is available from the SCADA data, and therefore the horizontal speed of the blades at any location along the span is known for the entire time history.

3.1.4. Blade cross section

Fig. 5 details the cross section of a blade under the defined axes system and with relevant moments shown. The two key bending moments which are computed directly from the strain data, the flapwise and edgewise moments, are shown. The blades rotate in the global Y-Z plane with rotational speed ω and horizontal velocity $v = r\omega$. The blades rotation in the negative local y-direction creates the horizontal velocity which, when added with the incident wind vector, create the apparent wind vector W.

3.1.4.1. Pitch angle. The pitch angle of a blade allows for the control of lift and drag forces on the blades (and therefore the hub speed) by varying the angle of attack. By changing the pitch angle, the turbine control system can optimize power generation according to control strategies based on wind speed. Forces and moments (such as flapwise and edgewise bending moments) which act according to the chord line's direction can be resolved into the local x-y axes of the blades as a function of the pitch angle. Figs. 6 and 7 have been produced from the available SCADA data from the Clipper turbine and describe the pitch angle and hub speed as a function of wind speed.

3.1.4.2. Wind direction. The wind turbine's yaw angle is reset automatically when the turbine nacelle (running along the X-axis in our reference system) reaches a maximum misalignment of 8° from the wind direction. For simplicity, in this paper the wind direction is assumed coincident with the X-axis of the turbine.

Table 2
Turbine property comparison.

Property	Clipper C96–2.5	NREL WindPACT 3.0	% Difference
Power Rating	2.5 MW	3.0 MW	+20%
Rotor Diameter, D	96 m	99 m	+3.0%
Swept Area, A_2	7328 m^2	7698 m^2	+5.0%
Rated Wind Speed, U_R	12 m/s	11.2 m/s	−6.7%
Blade length, R	46.7 m	47.025 m	+0.7%
Power Coefficient, C_p	0.326	0.453	+39%
Efficiency, η	0.550	0.764	+39%

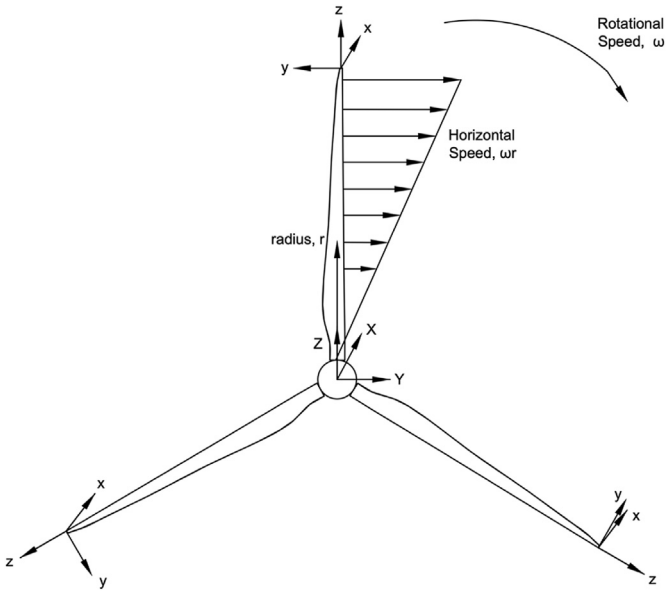

Fig. 4. Local and global coordinate systems and rotational speed of blades.

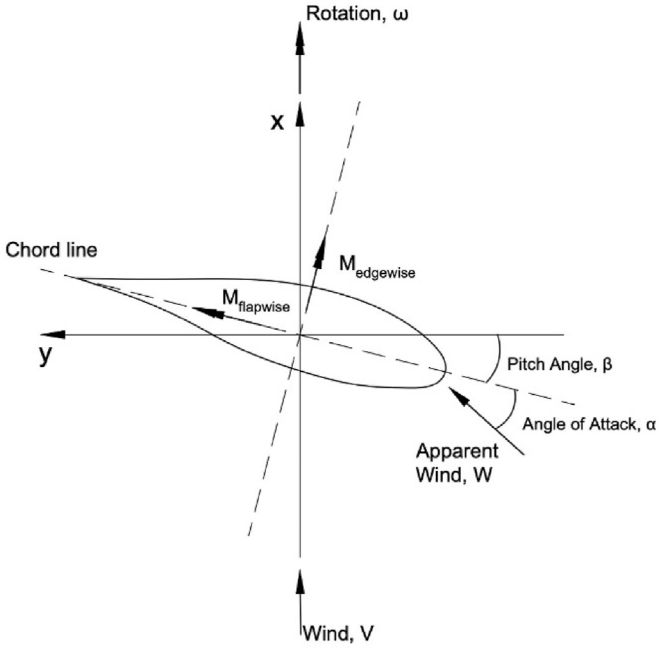

Fig. 5. Blade cross section displaying pitch angle, angle of attack, flapwise and edgewise moments.

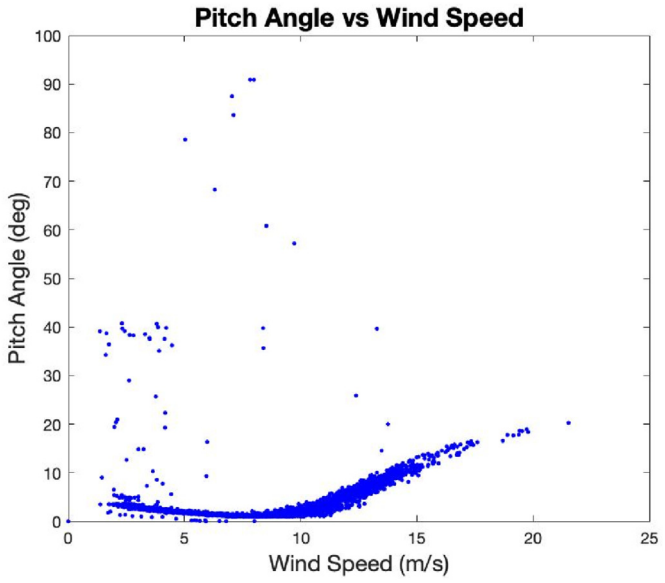

Fig. 6. Pitch angle vs wind speed (10 min average).

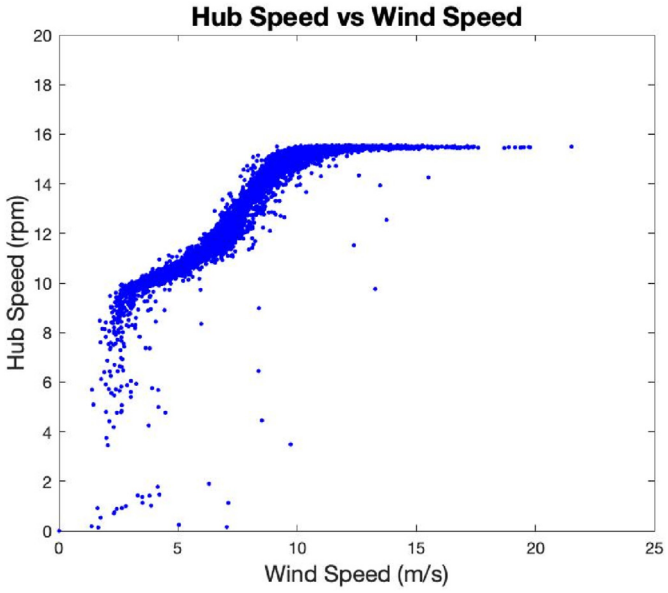

Fig. 7. Hub speed vs wind speed (10 min average).

The resultant apparent wind speed, W, is composed of the absolute wind speed and the horizontal wind speed produced by the blade rotation. This resultant apparent speed acts on the airfoil shape of the blades with an angle of attack, α, producing the lift and drag forces. Fig. 5 shows all the components and the resultant speed, and the magnitude of W is obtained by using Equation (1).

$$W = \sqrt{V^2 + (\omega r)^2} \tag{1}$$

where ω is the rotation speed and r is the length along the blade measured from the center of the rotor hub (See Fig. 4). V is the incident wind flow in the X-direction and is obtained from SCADA data. The direction of W, computed geometrically, acts with an angle of attack, α, between itself and the chord line of the airfoil cross section.

3.1.5. Lift and drag forces

For this work, two distances d_D and d_L are defined as the distances at which resultant forces for the lift and drag distributions act along the blade during operation. These distances are key properties used to calculate the shear forces on the blades (Section 3.2.2), but the estimation of the distances themselves is discussed here. The determination of these distances was done under a range of wind speeds to ensure the distances d_D and d_L do not vary significantly with wind speed.

The distances d_D and d_L are computed by estimating the lift and drag distributions along the span of the blade under the range of wind speeds and finding the location of a resultant force which would cause the same root bending moment. The specific blade profile detailing the airfoil shape and chord length along the blade is required to estimate the lift and drag force distributions. The profile of the Clipper blades is not provided by manufacturers and had to be inferred by referencing NREL's 3 MW reference wind turbine [21], which provides a detailed blade profile as described in Table 3. Calculations for lift and drag distributions were done on the NREL reference turbine, and the resulting distances d_D and d_L are scaled to the length of the Clipper C96 2.5 MW blade.

In Table 3, the chord length and airfoil cross section are defined at each location described by RNodes, which are evenly spaced nodes along the span of the NREL reference turbine blade. Under the Airfoil column, standardized airfoils are determined as the cross section at each node along the blade.

From SCADA data, several points of varying wind speed were chosen, and the corresponding pitch angle and hub speed at these points was noted. Wind speeds were chosen to reflect the range of wind speeds the turbine operates under, and to favor those that occur more commonly. It was verified that each point chosen was in the expected range of pitch speed and hub speed based on the wind speed (see Figs. 6 and 7).

To obtain the lift and drag distributions along the blade at the chosen wind speeds, the horizontal speed of the blades, equal to ωr, was computed, and following the relationship described in Fig. 8 and Equations (2) and (3), the angle of attack, α, at each node along the blade span is computed based on the incident wind flow, horizontal speed of the blades, and the pitch angle. Thus, for each wind speed under consideration and at each node along the blade, the angle of attack is known.

$$\varphi = \tan^{-1}\left(\frac{V}{\omega r}\right) \tag{2}$$

Table 3
NREL reference turbine blade properties for WindPACT 3 MW model [27].

Node	Rnodes (m)	Chord (m)	Airfoil
1	4.043	2.756	cylinder.dat
2	7.178	3.209	s818_2703.dat
3	10.313	3.662	s818_2703.dat
4	13.44750	3.880	s818_2703.dat
5	16.58250	3.646	s818_2703.dat
6	19.71750	3.412	s818_2703.dat
7	22.85250	3.178	s818_2703.dat
8	25.98750	2.944	s825_2103.dat
9	29.12250	2.710	s825_2103.dat
10	32.25750	2.476	s825_2103.dat
11	35.39250	2.242	s825_2103.dat
12	38.52750	2.018	s825_2103.dat
13	41.66250	1.808	s825_2103.dat
14	44.79750	1.597	s826_1603.dat
15	47.93250	1.386	s826_1603.dat

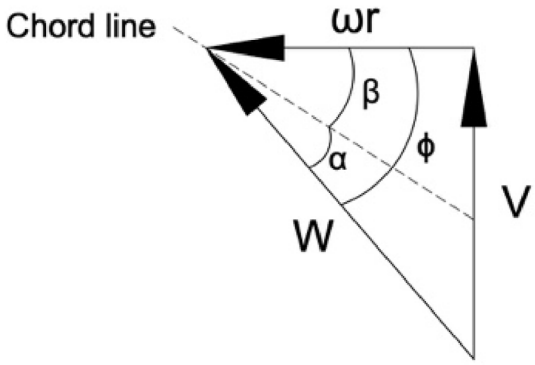

Fig. 8. Computation of angle of attack.

$$\alpha = \varphi - \beta \tag{3}$$

where β is the pitch angle and is available in SCADA data.

Lift and drag coefficients are used to compute the lift and drag forces acting on an airfoil. These coefficients for standardized airfoils can be found on database profiles [29] as a function of angle of attack, air density and Reynold's number. For each wind speed at a specific air density and assuming a Reynold's number range, the lift and drag coefficients C_L and C_D were estimated based on the angles of attack computed at each node along the span of the blade. Once the lift and drag coefficients for each point are known, the lift and drag forces acting at each node along the span of the blade can be calculated using the relative velocity, W, and the chord distance, c, according to Equations (4) and (5).

$$L = \frac{1}{2}\rho W^2 C_L c \tag{4}$$

$$D = \frac{1}{2}\rho W^2 C_D c \tag{5}$$

These calculations result in lift and drag force distributions along the blades for each wind speed considered. From these distributions, the application point of resultant lift and drag forces, defined as d_D and d_L, can be computed as explained in Fig. 9. The distances are computed by finding the distance at which an equivalent resultant lift or drag force would act to cause the same bending moment as the lift or drag force distributions. Different wind speed conditions were analyzed and the obtained distances d_L and d_D were found from the force distributions estimated as described above. The results are described in Table 4.

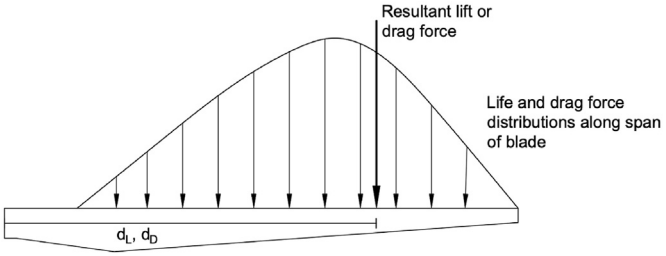

Fig. 9. Application point of lift and drag equivalent forces.

Table 4
Results of lift and drag application point computation.

Wind Speed (m/s)	Lift Distance, d_L (m)	Drag Distance, d_D (m)
4.9	30.9	27.1
6.0	32.7	25.6
10.0	32.4	25.6
14.0	30.5	23.2
Average Distance	31.7	25.4
Scaled length to Clipper blade	30.3	24.1

3.2. Estimation of forces at blade roots

3.2.1. Flapwise and edgewise bending moments

Two key bending moments can be calculated directly from the strain data due to the placement of the sensors at the High Pressure, Low Pressure, Leading Edge, and Trailing Edge positions. The flapwise and edgewise moments are calculated from the temperature compensated strain data as described by Equations (6) and (7). Fig. 10 shows the physical directions of these bending moments on the blades. These moments are later resolved into the local blade axes defined for our analysis.where k_1 and k_2 are constants provided as the sensor calibration factors and are based on the specific material and geometry of each blade, and $\varepsilon_{HP}, \varepsilon_{LP}, \varepsilon_{LE}, \varepsilon_{TE}$ are the temperature compensated strain measurements.

3.2.1.1. Bias correction in bending moment measurements. The flapwise and edgewise bending moments are the basis for all calculations of blade root reaction forces. These moments are expected to be of the same magnitude for each blade, however this is not seen in the moments computed from strain data, indicating some sort of bias in the data caused by sensor calibration or temperature compensation. The biases in strain data are suspected to cause a shift in the bending moments to incorrect magnitudes. The inconsistencies in the strain readings between blades are due to issues with the strain calibration. The authors did not have comprehensive information on the origins of these calibration factors, so first principles were applied to the measurements to gain more sensible readings.

To correct the bias, the bending moments were studied during a data set which showed slow rotation due to a high pitch angle of around 80°. At times like this during operation, the lift and drag forces are low as compared to the effect of blade weight in the

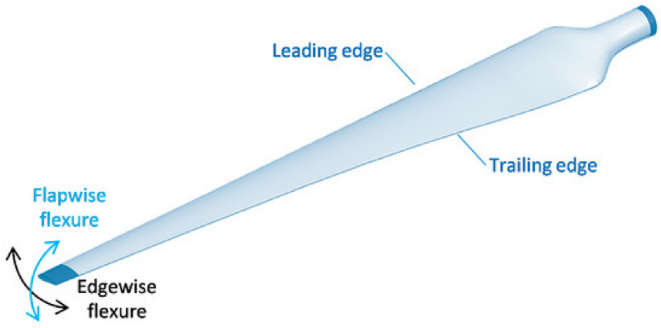

Fig. 10. Directions of flapwise and edgewise bending moments on a turbine blade [30].

$$M_{Flapwise} = (\varepsilon_{HP} - \varepsilon_{LP}) \cdot k_1 \tag{6}$$

$$M_{Edgewise} = (\varepsilon_{LE} - \varepsilon_{TE}) \cdot k_2 \tag{7}$$

bending moments. Fig. 11 shows the data from all three blades during the time-period used for estimation and correction of the measurement bias. This figure shows the transition from normal operation to a slow rotation due to the change in pitch angle and a resulting slower hub speed. The pitch angle and hub speed are obtained from the SCADA data.

As the rotor slows due to a drastic change in pitch angle, the component of weight contributing to the edgewise moment lessens, while the component contributing to the flapwise moment is increased. Therefore, such a period is utilized to correct the biased strain data.

In theory, parked conditions (i.e., pitch angle of 90) would have been preferred to estimate the expected bending moments due primarily to blade weight, since the lift and drag forces would be even lower during parked conditions. However, in parked conditions there is no rotation and therefore the blade azimuth angle is impossible to establish.

Given the pitch angle, azimuth angle, blade weights, and centers of gravity, the expected gravity-induced bending moments (assuming negligible lift or drag forces) are analytically reconstructed over the time-period shown in Fig. 11 for all three blades. In addition, the turbine tilt angle is considered for the full component reconstruction. The tilt angle is assumed to be 5° in this study, which is a typical value for turbines of this dimension.

The gravity-induced moments were computed using just the blade weights and centers of gravity, assuming only the blade weights were significantly contributing to the bending moments, while lift and drag forces are negligible. These reconstructed bending moments are computed according to Equations (8) and (9), where $(mg)_{flap}$ and $(mg)_{edge}$ are the components of blade weight acting in these directions (a function of azimuth angle and pitch angle), and the bending moments are therefore these components of force multiplied by the center of gravity distance. Fig. 12 displays the components of blade weight in the flapwise and edgewise directions.

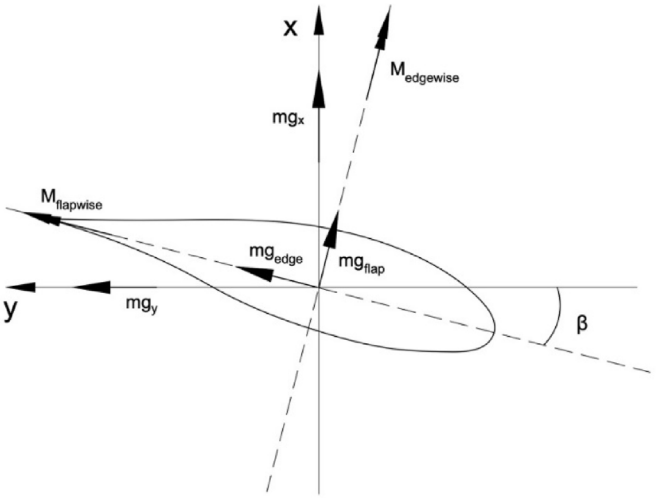

Fig. 12. Cross section view of blades with components of blade weight resolved into flapwise and edgewise directions.

$$M_{Flapwise,\ reconstructed} = (mg)_{flap} d_{CoG} \tag{8}$$

$$M_{Edgewise,reconstructed} = -(mg)_{edge} d_{CoG} \tag{9}$$

The analytically computed bending moments are compared to the measured ones in Fig. 13. Bias for each of the bending moments is estimated so the bias-corrected (shifted) moments match their analytically computed counterparts at this period. Fig. 13 shows the applied bias correction and the shift to one of the blades based on its reconstructed bending moments, which are overlayed on the graph. This was done for each blade, resulting in a different shift magnitude for each blade's two bending moments. The required shift magnitude estimated through this analysis for each of the bending moments on each blade was then applied to all data sets.

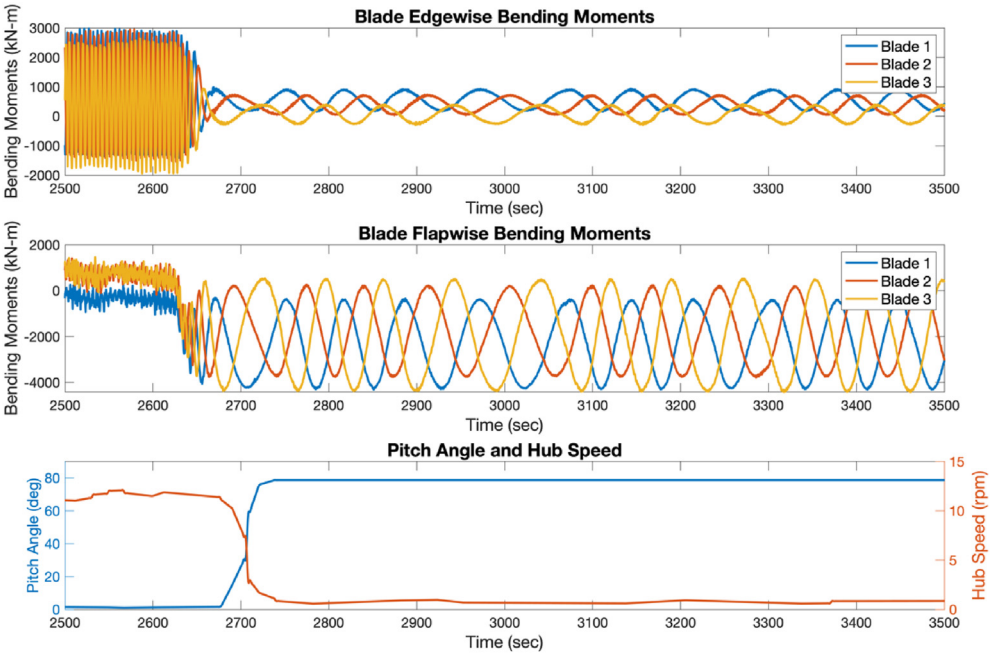

Fig. 11. Data set utilized in bias analysis.

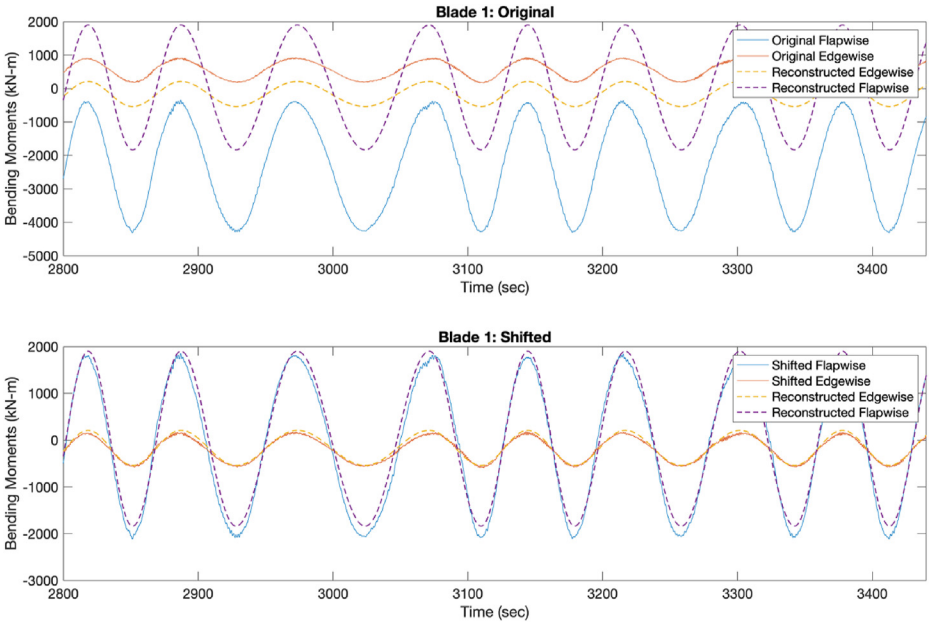

Fig. 13. Example of shift applied to bending moment data.

Table 5 details the magnitudes of shift applied to the blades' flapwise and edgewise bending moments.

Fig. 14 shows the bending moments before and after the bias correction as a function of wind speed, taken as 10-min averages from all available data sets. Overlayed on this is the bending moments computed in an OpenFAST simulation of the NREL 3 MW reference turbine (see Sections 3.1.1 and 5). This is believed to be a justifiable correction due to the close match in amplitude of the measured and reconstructed bending moments as well as the match seen between resulting measured bending moment magnitudes and OpenFAST simulation on a similarly sized turbine. The resulting bending moment magnitudes as a function of wind speed are also in close agreement among the three blades, although small differences are noticed which are likely caused by inaccurate sensor calibration factors. These differences cannot be corrected from our data but are considered small in relation to the analyses performed. Fig. 15 shows an example of the measured flapwise and edgewise moments for one of the blades after correction for bias.

3.2.1.2. Blade azimuth angle. The azimuth angle, Φ, which describes a blades rotation around the rotor hub, is an important measurement used in conducting blade force calculations. The flapwise and edgewise bending moments which can be computed directly from the strain gauges (as discussed in Section 4.1), were used to estimate the azimuth angle. Due to rotation around the rotor hub, the blade weight produces cyclical forces which are seen most clearly in the edgewise bending moment as explained in Figs. 16 and 17. When the blade is out at 90 or 270°, the bending moment is at its maximum magnitude, due to the components of blade weight contributing to the bending moment. The blade azimuth angle is therefore inferred from the peaks and valleys of the bending moment time history and is assumed to change linearly during rotation. Resulting rotational speeds based on the computed angles were compared to rotation speeds from the SCADA data, and they matched closely.

Table 5
Shift in flapwise and edgewise moments by blade.

	Flapwise Shift (kN-m)	Edgewise Shift (kN-m)
Blade 1	+2200	−775
Blade 2	+1950	−600
Blade 3	+2000	−200

3.2.2. Root reaction forces and moments

The sensor data from the blades cannot provide direct calculations of shear forces because the sensors are placed along the axial direction, in the direction of the z-axis, and the shear root reaction forces in local coordinates are in the x and y axes. The blade root reaction forces during operation are caused by the applied shear forces on the blades due to wind flow and the blade weights. In other words, lift and drag shear forces due to wind flow over the blades coupled with the effect of blade weight cause the flapwise and edgewise bending moments. Lift and drag forces cannot be computed directly as the blade profile is not available. However, since the flapwise and edgewise moments and the weight of the blades are known, the magnitude of the lift and drag forces can be estimated.

The effective lift and drag forces are defined as the resultant forces of lift and drag force distributions along the blades, and the location of these effective point loads was computed in Section 3.5 as d_L and d_D. The weights and centers of gravity of each blade are known and provided in Table 6. To estimate the effective lift and drag forces, the components of blade weight contributing to the flapwise and edgewise moments must first be computed. To do this, the blade weights acting downward must be resolved into the local axes of the blades. First, the blade weight is resolved into the x-axis and the y-z plane as a function of the tilt angle, assumed here to be 5°, as shown in Fig. 18 and Equations (10) and (11). The component acting in the y-z plane is further resolved into the y and z-axes as a function of the blade azimuth angle, Φ, as shown in Fig. 19 and Equation (12). Only the weight which acts in the local x and y-axes of each blade is relevant to this analysis, as the z-axis is in the axial direction and this component of blade weight does not contribute to the edgewise and flapwise bending moments.

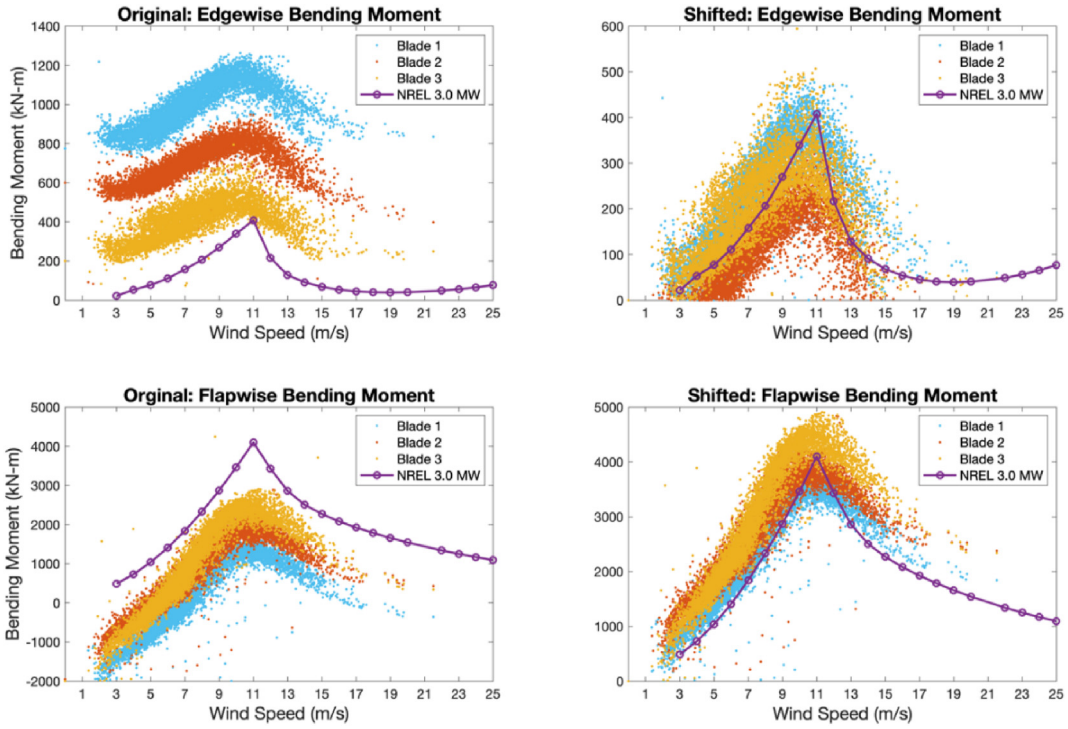

Fig. 14. Bending moments before and after shift due to bias.

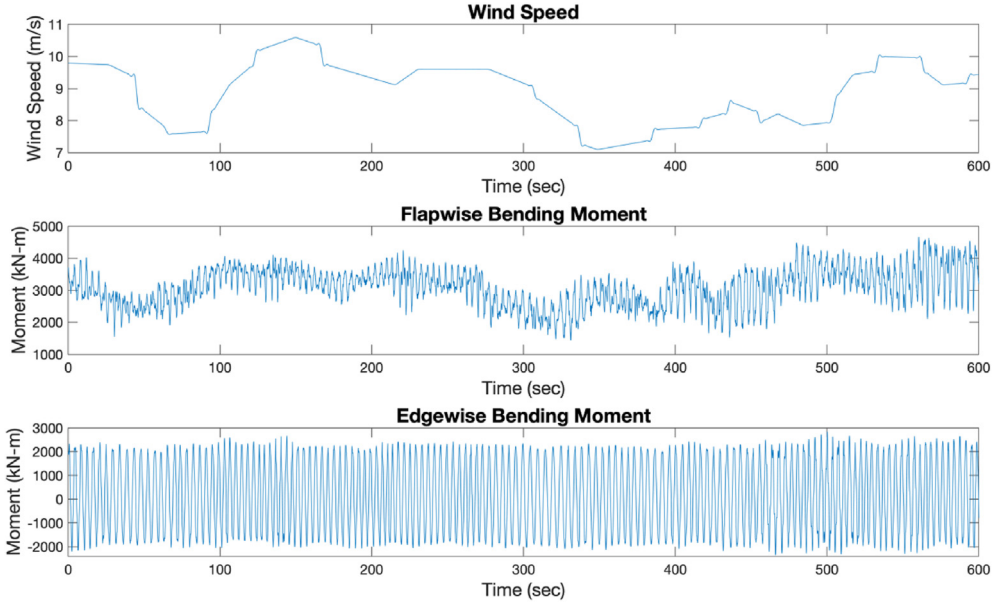

Fig. 15. Example flapwise and edgewise bending moments after bias correction.

$$(mg)_x = (mg)\sin(\alpha_t) \tag{10}$$

$$(mg)_{yz} = (mg)\cos(\alpha_t) \tag{11}$$

$$(mg)_y = -(mg)_{yz}\sin(\Phi) \tag{12}$$

Once the weight is resolved into the x and y axes, $(mg)_x$ and $(mg)_y$ are further resolved into the flapwise and edgewise directions because these components act in the plane of the cross section of the blade. This is based on the pitch angle and is shown as $(mg)_{edge}$ and $(mg)_{flap}$ in Fig. 19. These forces act at the center of gravity d_{CoG} of each of the blades as defined in Table 6 and shown in Fig. 20.

Figs. 20 and 21 also show the effective lift and drag forces defined for these calculations which are shown as $F_{lift,\,eff}$ and $F_{drag,\,eff}$ acting at distances d_L and d_D respectively. $F_{drag,eff}$ and $F_{lift,eff}$ are computed by defining the flapwise and edgewise moments as moments which are caused solely by the lift and drag forces from wind plus the weight of the blades. These forces are computed

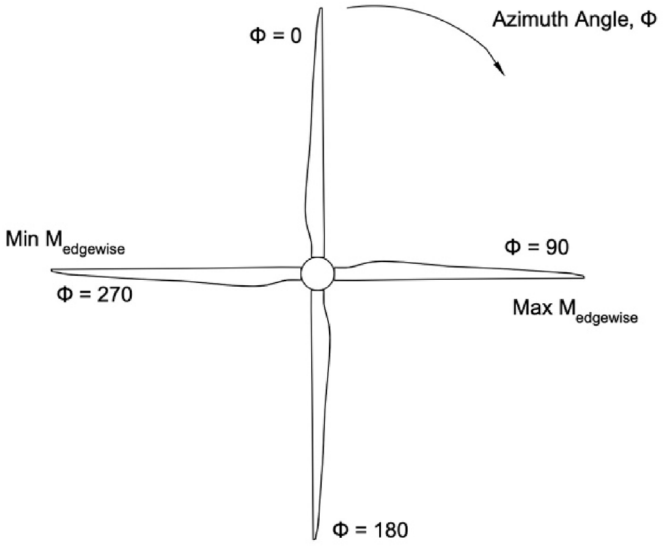

Fig. 16. Magnitudes of edgewise moment cycles based on blade rotation.

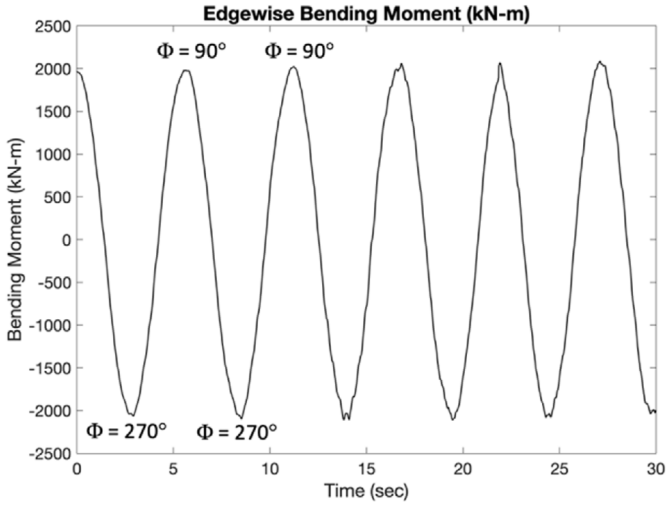

Fig. 17. Blade angles based on magnitude of edgewise moment.

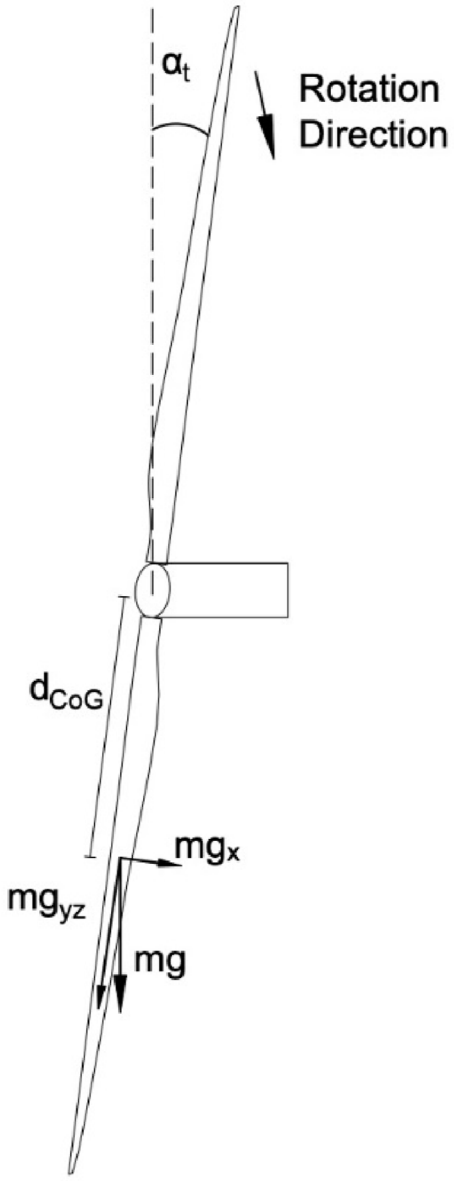

Fig. 18. Blade weight resolved into plane of rotation as function of tilt angle.

Table 6
Blade weights and centers of gravity.

	Weight (kg)	d_{CoG} (m)
Blade 1	12,201	15.995
Blade 2	12,313	15.850
Blade 3	12,552	15.548

using Equations (13) and (14), which define the bending moments in this way.

$$M_{Flapwise} = (mg)_{flap} d_{CoG} + F_{lift,eff} d_L \tag{13}$$

$$M_{Edgewise} = -(mg)_{edge} d_{CoG} - F_{drag,eff} d_D \tag{14}$$

Once $F_{lift,\ eff}$ and $F_{drag,\ eff}$ are computed, the root reaction shear forces on the blade can be computed according to the directions of these forces as shown in Figs. 20 and 21. These forces are root reaction force due to weight forces and lift or drag forces. This is done according to Equations (15) and (16).

$$F_{flap} = (mg)_{flap} + F_{lift,eff} \tag{15}$$

$$F_{edge} = (mg)_{edge} + F_{drag,eff} \tag{16}$$

The root reaction forces on the blade are resolved into the local defined axes of the blades as a function of pitch angle. Similarly, flapwise and edgewise bending moments are resolved into the x-y axis. Fig. 22 defines the directions of these forces which are consistent with the coordinate axes utilized by OpenFAST simulations and models.

$$F_x = F_{edge} \sin\beta + F_{flap} \cos\beta \tag{17}$$

$$F_y = F_{edge} \cos\beta - F_{flap} \sin\beta \tag{18}$$

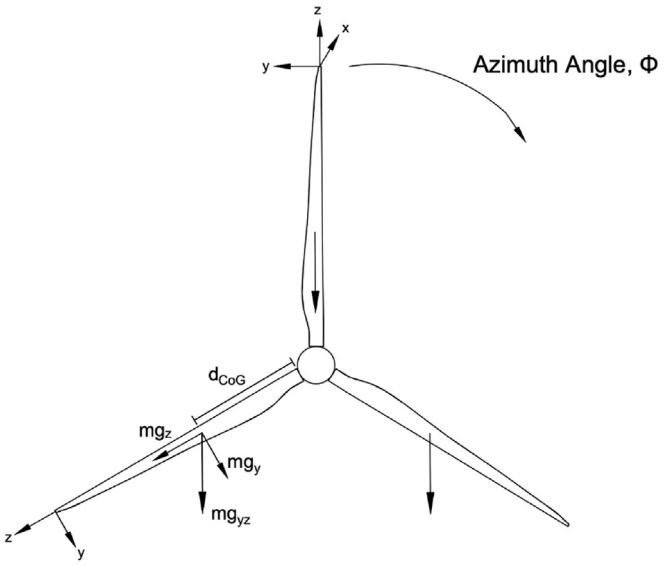

Fig. 19. Blade weight resolved into local blade axes as function of azimuth angle.

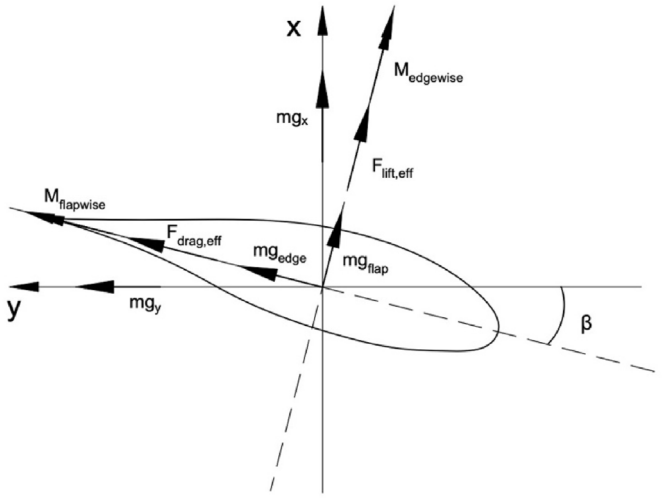

Fig. 20. Flapwise and edgewise bending moment contributing forces.

$$M_x = M_{Edgewise}\cos\beta + M_{Flapwise}\sin\beta \tag{19}$$

$$M_y = -M_{Edgewise}\sin\beta + M_{Flapwise}\cos\beta \tag{20}$$

4. Comparison to NREL guidelines

The NREL reference wind turbine report provides graphs of certain forces and other parameters of the turbine during operation as a function of wind speed [27]. These include parameters such as rotor speed, pitch angle, and tip speed ratio (TSR), and the rotor thrust force and rotor torque. The graphs produced by NREL are shown in Fig. 23. Fig. 24 graphs the parameters and forces computed from the strain sensors and SCADA data in this study for comparison with NREL reference turbine values.

Rotor thrust for the Clipper 2.5 MW turbine is computed through a rigid body equilibrium analysis by resolving the forces

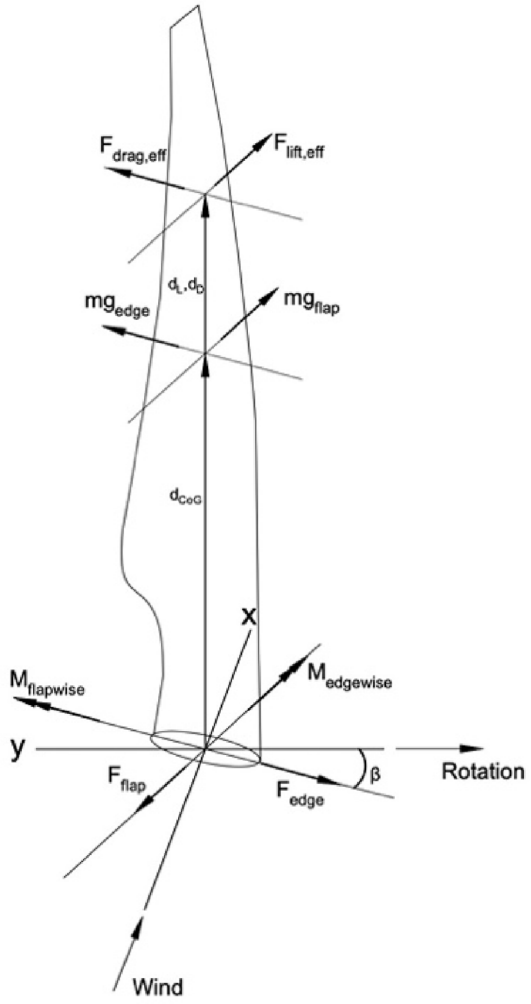

Fig. 21. Bending moment contributing forces and root reaction shear forces.

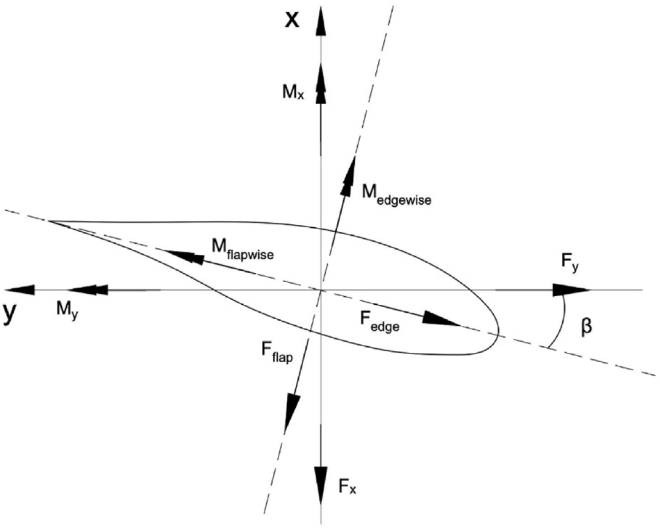

Fig. 22. Root reaction forces and moments resolved into local axes.

from each of the blades onto the main shaft as a function of blade azimuth angle. The comparison of rotor thrust values shows that

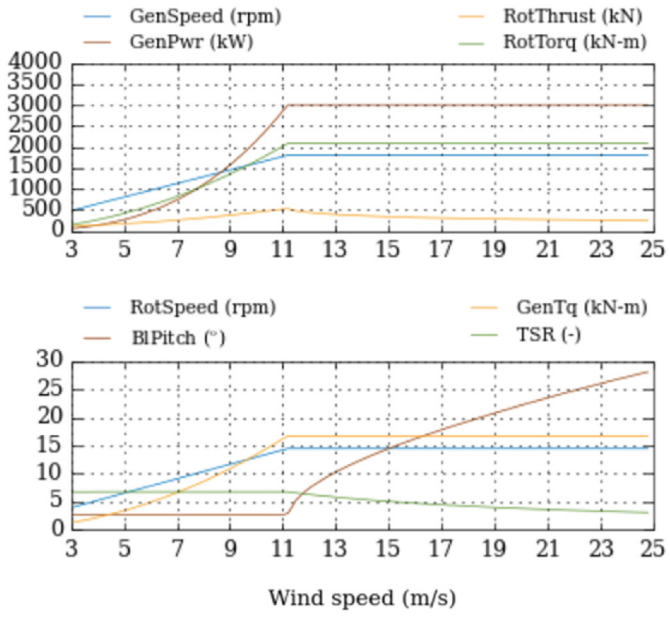

Fig. 23. NREL 3 MW reference turbine parameters [27].

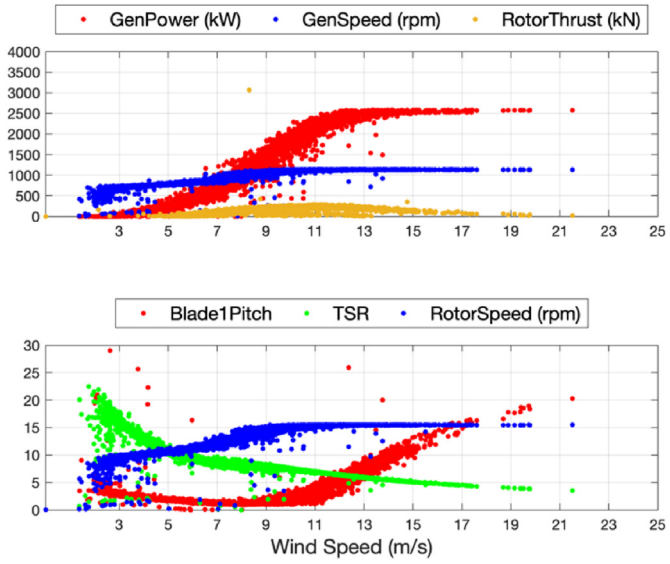

Fig. 24. Parameters computed based on strain data and scada data for the clipper 2.5 MW Turbine.

while our values are slightly lower in magnitude, the shape of the force as a function of wind speed is similar. In both cases, rotor thrust rises until approximately 11 m/s, the rated wind speed of the NREL 3 MW reference turbine, before declining again. This aligns well with the observed rotor thrust shape for the Clipper turbine, as the rated wind speed for the Clipper 2.5 MW turbine is 12 m/s. The slight differences in shape and lower magnitude of rotor thrust could be explained by the different rated wind speeds, and the fact that the Clipper turbine is smaller in both size and output. In fact, the rotor thrust magnitudes computed for the Clipper 2.5 MW turbine here fall somewhere between rotor thrust values for the NREL 1.5 MW and 3.0 MW reference turbines.

Other parameters such as rotor speed, pitch angle and TSR compared here come from the SCADA data directly or are calculated using parameters in the SCADA data. These parameters match the reference turbine well, as they are products of the control system on the turbine and independent of the calculations in this paper. These parameters, in particular the rotor speed, match the reference turbine closely, which serves as confirmation that using the 3 MW turbine as reference for this Clipper 2.5 MW is a reasonable assumption.

5. Results

The NREL 3 MW WT has also been modeled in OpenFAST [31] for a more detailed comparison of the forces and moments computed in this paper.

OpenFAST is a multi-physics tool for the dynamic simulation of wind turbines. OpenFAST includes computational modules for aerodynamics, control and electrical systems, structural dynamics, and hydrodynamics for offshore turbines. The modules work together to create coupled nonlinear simulations in the time domain. The inputs can be altered to run a range of simulation settings and conditions. The most important modules that are included in the program which work together to simulate the whole turbine includes ElastoDyn (structural dynamics module), BeamDyn (finite element blade structural dynamics), AeroDyn (aerodynamics), InflowWind (wind inflow conditions), and ServoDyn (control and electrical drive dynamics). More details about the OpenFAST modules and solvers can be found in Ref. [31].

The NREL 3 MW was simulated at steady wind speeds between 3 and 25 m/s. OpenFAST allows for the output of all root reaction forces and moments on the blades. These parameters have been obtained for each wind speed by taking the average value from a 10-min-long simulation under steady wind conditions. Steady wind indicates that the wind speed is constant during the simulation and that there is no turbulence or gusts.

The OpenFAST files available for the NREL 3 MW WT were not available for the most recent version of OpenFAST and had to be updated by the authors. Fig. 25 has been reproduced for this study to ensure that the simulations being studied here are consistent with the NREL report for the 3 MW turbine. Fig. 25 can be compared to Fig. 23, which has been obtained directly from the NREL

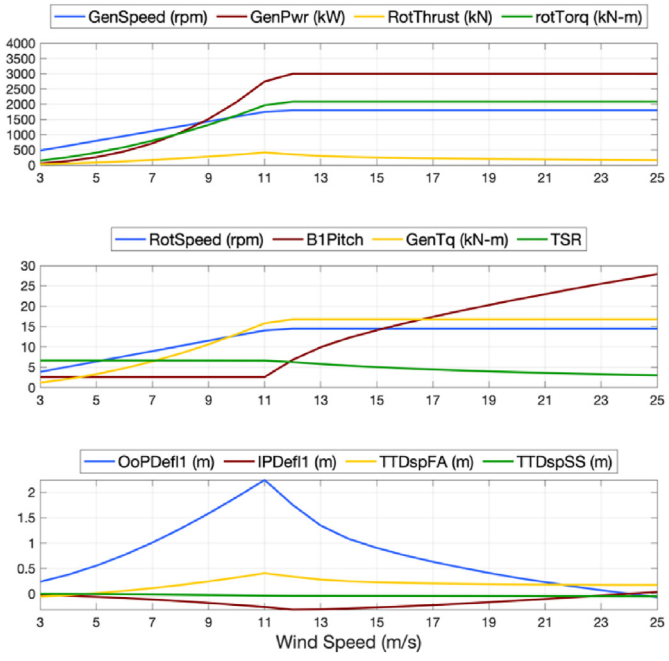

Fig. 25. Openfast simulation results for comparison with NREL Report, 3 MW turbine.

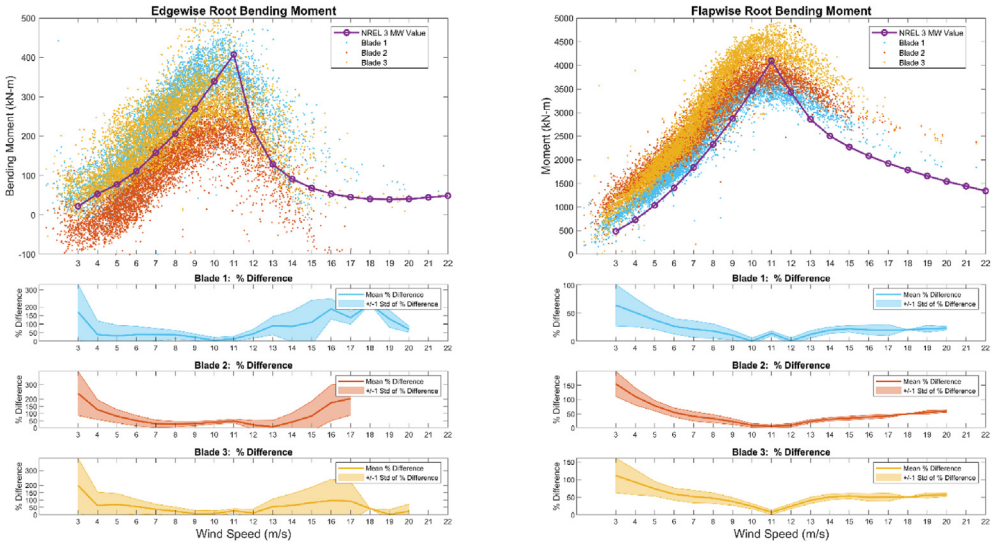

Fig. 26. Comparison of edgewise and flapwise bending moments.

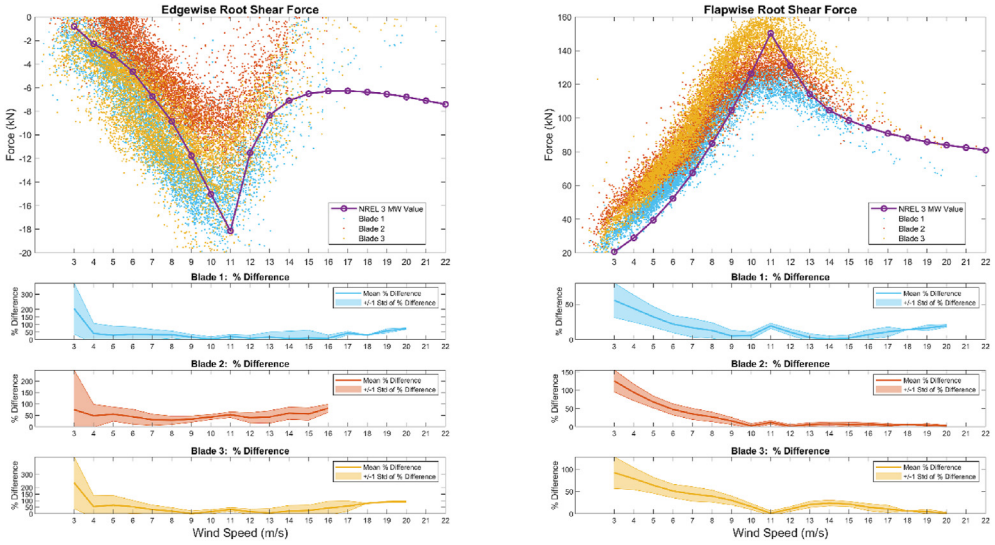

Fig. 27. Comparison of edgewise and flapwise shear reaction forces.

WindPACT reference turbine report [27]. The match between the OpenFAST outputs in Fig. 25 and the NREL reference turbine report in Fig. 23 indicate that the simulations are running correctly.

Figs. 26–29 display the comparisons between OpenFAST outputs and the forces and moments derived in this paper. Beneath these plots are the percent difference values between the derived forces/moments from Clipper measurements and their counterparts estimated from the NREL reference turbine model in OpenFAST. OpenFAST output values are simulated at integer wind speed values from 3 to 25 m/s, and Clipper turbine values are placed into bins of wind speed at integer values with ranges of ± 0.5 m/s from each integer. Overall, the estimated forces and moments match the trend of their model-simulated counterparts.

It can be observed that in general the data-driven values are in good agreement with model simulations at the rated wind speed (12 m/s) and the range of 8–13 m/s. This can be related to the fact that (a) we expect smaller modeling errors at the rated wind speed and close to it, and (b) there are fewer data points representing high wind conditions of >13 m/s. Comparison is limited at high wind speeds by the lack of data sets from the Clipper turbine operating at these speeds, but the trend of most results indicate that the data continues to match expected shapes and magnitudes. For example, in Fig. 29 the shape of the M_x reaction moment seems to extend horizontally into higher wind speeds, as is also seen in the OpenFAST simulation results. This can be seen in several other comparisons.

The variance in the Clipper data is expected due to varying environmental conditions and other parameters. Measurements of a turbine's operation is a function of numerous features, many of which are not measured by the SCADA data, and many still not fully understood. Results show that the percent difference is correlated with the variation in the data, indicating that the high variance in the data is a major source of the error when we compare the Clipper turbine to steady wind speeds on the NREL turbine. This is to be expected, and it should be stressed that the variance is normal, and the NREL OpenFAST outputs are an idealized simulation of the turbine. The OpenFAST simulation values at steady wind speeds are not realistically going to apply to all environmental conditions that

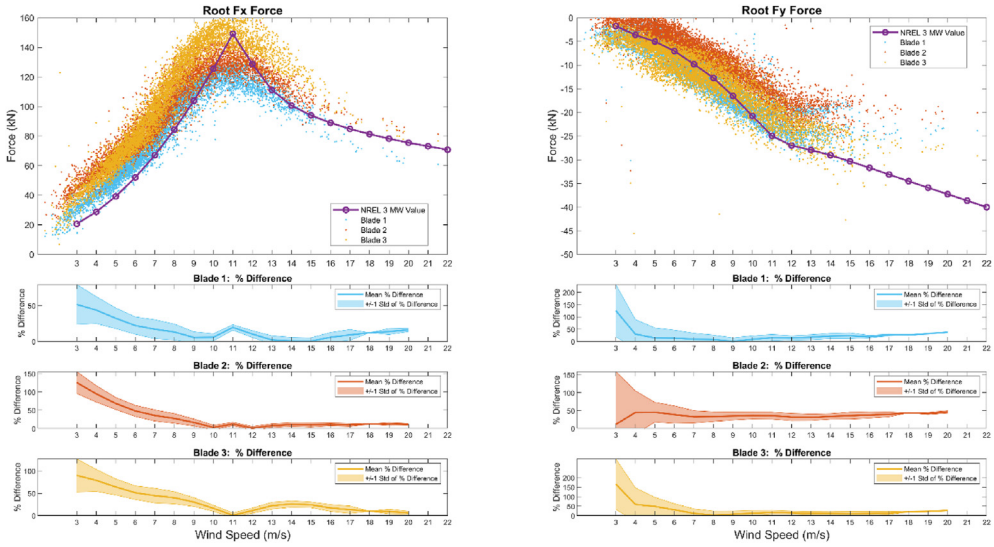

Fig. 28. Comparison of root reaction forces in local axes of blade.

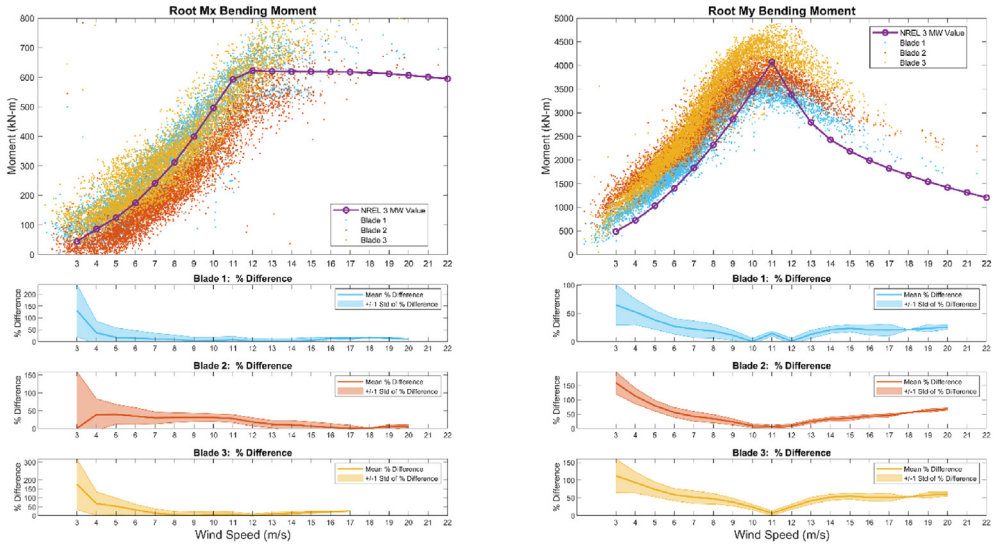

Fig. 29. Comparison of root reaction bending moments in local axes of blade.

the Clipper data represents.

It is worth noting that the OpenFAST simulations for the NREL turbine were run under steady wind conditions, with no turbulence or other variation in environmental conditions. This is because the SCADA data does not provide wind turbulence or many other relevant environmental conditions, as it would not be possible to model the NREL turbine under the exact same conditions that are seen in the Clipper dataset. Still, the NREL steady wind speed readings consistently fall within the range of values seen in the Clipper data.

In addition to environmental conditions, another parameter which will cause variation is the controls of the turbine. Differences in forces and moments between two turbines are enhanced by differences in the control algorithms of the turbines. For example, the pitch angle has a major effect on the direction in the blade that forces will act. As can be seen in bottom subplots of Figs. 23 and 24, the pitch control for the Clipper and the NREL turbines is not the same. Furthermore, the pitch angle of Clipper turbine shows relatively large variations at each wind speed as opposed to a single pitch value at each wind speed seen in the NREL model. This is another source of variation in the Clipper data, as well as differences between the Clipper and the OpenFAST results.

6. Conclusions

The methods detailed in this paper allow for the computation of blade-root reaction forces and moments based on strain measurements taken at the blade roots and by using parameters of an NREL reference turbine of a similar size to replace structural design details not available to the public. This analysis was done using strain gauge and SCADA data from a Clipper 2.5 MW onshore turbine. Initial results show that this method is a viable way to estimate the blades' forces and moments, as the comparison of results show a close match with the same forces on the NREL 3 MW reference turbine according to OpenFAST simulations.

Discrepancies in this comparison may be due to the difference in size and output capacities of the Clipper 2.5 MW turbine considered in this paper and the NREL 3 MW WindPACT reference turbine.

In particular, the different control algorithms for the turbines serves as an added source of variability and difference between forces and moments. Additionally, real world data from the Clipper turbine has many other sources of variance in the dataset, which is expected. The OpenFAST simulations cannot recreate the exact conditions that the Clipper turbine experienced during the time-periods of available data, and many of these conditions are not measured by the Clipper dataset. Still, NREL 3 MW simulation output values fit very well into the range of values measured on the Clipper turbine.

Data availability

The data associated with this article is not publicly available and cannot be shared. Its usage in this article has been approved by the owner.

CRediT authorship contribution statement

Bridget Moynihan: Formal analysis, Investigation, Writing – original draft, Visualization. **Babak Moaveni:** Writing – review & editing, Supervision, Project administration. **Sauro Liberatore:** Writing – review & editing, Conceptualization. **Eric Hines:** Writing – review & editing, Supervision.

Declaration of competing interest

The authors declare that they have no known competing financial interests or personal relationships that could have appeared to influence the work reported in this paper.

Acknowledgments

The authors acknowledge partial support of this study by the National Science Foundation grant 1903972. The opinions, findings, and conclusions expressed in this paper are those of the authors and do not necessarily represent the views of the sponsors and organizations involved in this project.

References

[1] Wind Powers America Annual Report 2019, Executive Summary, American Wind Energy Association. https://www.awea.org/getattachment/Resources/Publications-and-Reports/Market-Reports/AMR2019_ExecutiveSummary/AMR2019_ExecutiveSummary_Download/AWEA_WPA_ExecutiveSummary2019.pdf.aspx?lang=en-US.
[2] SG 14-222 DD Offshore wind turbine, Siemens Gamesa Renewable Energy. https://www.siemensgamesa.com/en-int/-/media/siemensgamesa/downloads/en/products-and-services/offshore/brochures/siemens-gamesa-offshore-wind-turbine-brouchure-sg-14-222-dd.pdf.
[3] Haliade-X 12 MW offshore wind turbine platform, GE Renewable Energy. https://www.ge.com/renewableenergy/wind-energy/offshore-wind/haliade-x-offshore-turbine.
[4] Cuong D. Dao, Behzad Kazemtabrizi, Christopher J. Crabtree, Wind turbine reliability data review and impacts on levelised cost of energy, Wind Energy 22 (12) (2019) 1848–1871.
[5] Christopher A. Walford, Wind Turbine Reliability: Understanding and Minimizing Wind Turbine Operation and Maintenance Costs; Sandia Report No. SAND2006-1100, Sandia National Laboratories, Albuquerque, NM, USA, 2006.
[6] Pierre Tchakoua, René Wamkeue, Mohand Ouhrouche, F. Hasnaoui, Theubou Tameghe, Tommy Andy, Gabriel Ekemb, Wind turbine condition monitoring: state-of-the-art review, new trends, and future challenges, Energies 7 (2014) 2595–2630, https://doi.org/10.3390/en7042595.
[7] Renewable Energy Technologies: Cost Analysis Series. Volume 1: Power Sector, Issue 5/5, International Renewable Energy Agency, June 2012.
[8] M.D. Reder, et al., Wind turbine failures – tackling current problems in failure data analysis, J. Phys. Conf. 753 (2016), 072027, 2016.
[9] D.J. Pedregal, F.P. Garcia Marquez, C. Roberts, An algorithmic approach for maintenance management, Ann. Oper. Res. 166 (2009) 109e24.
[10] F.P. García Márquez, A.M. Tobias, J.M. Pinar Pérez, Condition monitoring of wind turbines: techniques and methods, Renew. Energy 46 (2012) 169–178.
[13] Kristof Maes, Alexandros Iliopoulos, Wout Weijtjens, Christof Devriendt, Geert Lombaert, Dynamic strain estimation for fatigue assessment of an offshore monopile wind turbine using filtering and modal expansion algorithms, Mech. Syst. Signal Process. 76 (2016), https://doi.org/10.1016/j.ymssp.2016.01.004.
[14] Alexandros Iliopoulos, Rasoul Shirzadeh, Wout Weijtjens, Patrick Guillaume, Danny Van Hemelrijck, Christof Devriendt, A modal decomposition and expansion approach for prediction of dynamic responses on a monopile offshore wind turbine using a limited number of vibration sensors, Mech. Syst. Signal Process. 68–69 (2016) 84–104, https://doi.org/10.1016/j.ymssp.2015.07.016. ISSN 0888-3270.
[15] Katharina Fischer, Diego Coronado, Condition monitoring of wind turbines: state of the art, user experience and recommendations, VGB PowerTech 2015 (2015) 51–56.
[16] C. Devriendt, F. Magalhaes, W. Weijtjens, G.D. Sitter, Á. Cunha, P. Guillaume, Structural health monitoring of offshore wind turbines using automated operational modal analysis, Struct. Health Monit. 13 (2014) 644–659.
[17] G. Oliveira, F. Magalhães, Á. Cunha, et al., Development and implementation of a continuous dynamic monitoring system in a wind turbine, *J Civil Struct Health* Monit 6 (2016) 343–353, https://doi.org/10.1007/s13349-016-0182-7.
[18] R. Rolfes, S. Tsiapoki, M. Häckell, M. Wang, J. Lynch, H. Sohn, Sensing solutions for assessing and monitor- ing wind turbines, in: Sensor Technologies for Civil Infrastructures - Applications in Struc- Tural Health Monitoring, Edts, Woodhead Publishing, 2014, pp. 565–604.
[19] İbrahim Sina Kuseyri, Condition Monitoring of Wind Turbines: Challenges and Opportunities, 2015.
[20] C. Liao, K. Shi, X. Zhao, Predicting the extreme loads in power production of large wind turbines using an improved PSO algorithm, Appl. Sci. 9 (2019) 521, https://doi.org/10.3390/app9030521.
[21] Luc Rademakers, ECN, Fibre Optic Load Monitoring of Wind Turbines, October 2012.
[22] Z. Hameed, Y.S. Hong, Y.M. Cho, S.H. Ahn, C.K. Song, Condition monitoring and fault detection of wind turbines and related algorithms: a review, Renew. Sustain. Energy Rev. 13 (Issue 1) (2009) 1–39, https://doi.org/10.1016/j.rser.2007.05.008. ISSN 1364-0321.
[23] M. Ovenden, Q. Wang, S. Huang, W. Zhao, S. Wang, June 6, Real-time monitoring of wind turbine blade alignment using laser displacement and strain measurement, ASME. ASME J Nondestructive Evaluation 2 (3) (2019), 031001, https://doi.org/10.1115/1.4043850. August 2019.
[24] Omar Mabrok Bouzid, Gui Yun Tian, Kanapathippillai Cumanan, David Moore, Structural health monitoring of wind turbine blades: acoustic source localization using wireless sensor networks, Journal of Sensors (2015), 139695, https://doi.org/10.1155/2015/139695, 11 pages, 2015.
[25] W. Yang, P.J. Tavner, C.J. Crabtree, M. Wilkinson, 'Cost-effective condition monitoring for wind turbines, IEEE Trans. Ind. Electron. 57 (1) (2010) 263–271.
[26] D. McMillan, G. Ault, Condition Monitoring Benefit for Onshore Wind Turbines: Sensitivity to Operational Parameters, IET Renewable Power Generation, April 2008.
[27] J. Rinker, K. Dykes, WindPACT Refereence Wind Turbines, National Renewable Energy Laboratory Technical, April 2018. Report NREL/TP-5000-67667.
[28] Liberty 2.5 MW wind turbine facts & specifications, Clipper Windpower Plc. Obtained from, https://geosci.uchicago.edu/%7Emoyer/GEOS24705/Readings/Liberty_Brochure_2009_LR.pdf.
[29] Airfoil Tools. airfoiltools.com.
[30] Y. Swolfs, Perspective for fibre-hybrid composites in wind energy applications, materials, Nobember (2017).
[31] OpenFAST web page, September, https://github.com/OpenFAST/openfast, 2020.